

Large eddy simulation of flow around a stay cable with an artificial upper rivulet

Yan Zhao¹, Xiaoqing Du^{*1,2}, Ming Gu³, Xiao Yang¹, Junjun Li¹ and Ping He¹

¹Department of Civil Engineering, Shanghai University, No. 99 Shangda Road, Shanghai, China

²Wind Engineering and Aerodynamic Flow Control Research Center, Shanghai University, No. 99 Shangda Road, Shanghai, China

³State Key Laboratory for Disaster Reduction in Civil Engineering, Tongji University, No. 1239 Siping Road, Shanghai, China

(Received March 28, 2017, Revised February 10, 2018, Accepted February 25, 2018)

Abstract. The appearance of a rivulet at the upper surface of a stay cable is responsible for rain-wind-induced vibration (RWIV) of cables of cable-stayed bridges. However, the formation mechanism of the upper rivulet and its aerodynamic effects on the stay cable has not been fully understood. Large eddy simulation (LES) method is used to investigate flow around and aerodynamics of a circular cylinder with an upper rivulet at a Reynolds number of 140,000. Results show that the mean lift coefficients of the circular cylinder experience three distinct stages, zero-lift stage, positive-lift stage and negative-lift stage as the rivulet located at various positions. Both pressure-induced and friction-induced aerodynamic forces on the upper rivulet are helpful for its appearance on the upside of the stay cable. The friction-induced aerodynamic forces, which have not been considered in the previous theoretical models, may not be neglected in modeling the RWIV. In positive-lift stage, the shear layer separated from the upper rivulet can reattach on the surface of the cylinder and form separation bubbles, which result in a high non-zero mean lift of the cylinder and potentially induces the occurrence of RWIV. The separation bubbles are intrinsically unsteady flow phenomena. A serial of small eddies first appears in the laminar shear layer separated from the upper rivulet, which then coalesces and reattaches on the side surface of the cylinder and eventually sheds into the wake.

Keywords: rain-wind-induced vibration; numerical simulation; upper rivulet; friction; separation bubble

1. Introduction

Stay cables of cable-stayed bridges often experience vibrations with large amplitudes induced jointly by both wind and rain due to their inherent characteristics of great flexibility, extremely low damping, and relatively small mass. Large-amplitude rain-wind-induced vibrations (RWIV) of cables were observed when both wind and rain are in presence (Hikami and Shiraishi 1988, Matsumoto *et al.* 1992, Main and Jones 1999, Shi *et al.* 2003, Ni *et al.* 2007, Zuo and Jones 2010, Acampora and Georgakis 2011). Cable vibration may cause undue stress on the cable in the vicinity of the anchorage, which potentially leads to fatigue fractures of internal wire strands or damage to the steel tubes protecting the cable at the bridge deck level. Therefore, to understand the mechanism and further mitigate the large-amplitude vibration has become a significant concern to bridge engineering and wind engineering communities.

Extensive research works have been conducted to investigate characteristics and the mechanism of RWIV in the past two decades. Many recent studies have indicated that the existence and the movement of the upper rivulet on the cable surface should be responsible for the instability phenomenon (Hikami and Shiraishi 1988, Yamaguchi 1990, Flamand 1995, Verwiebe and Rucheweyh 1998, Gu *et al.*

1998, Gu and Du 2005, Matsumoto *et al.* 2005, Xu *et al.* 2006, Gu *et al.* 2009). However, the precise excitation mechanism of RWIV remains unclear as information on the rivulet is inadequate (Jing *et al.* 2017).

Wind tunnel tests, theoretical analyses, and numerical simulations were used to investigate the characteristics of the upper rivulet and its effects on the RWIV by researchers. As for the wind tunnel tests, there are mainly two kinds of approaches to simulate the rain rivulet on a cable model and study the characteristics of the upper rivulet. One is to spray water appropriately on the surface of cable models to form a rivulet (Hikami and Shiraishi 1988, Cosentino *et al.* 2003, Gu and Du 2005, Li *et al.* 2010, Jing *et al.* 2015, 2017). The position of the upper rivulet during RWIV has been observed under the influence of wind speed, cable inclination and wind angle (Hikami and Shiraishi 1988, Gu and Du 2005). The geometry of the rivulet was measured in the tests by Cosentino *et al.* (2003) and Li *et al.* (2010). The circumferential movement of the rivulet and its relationship with the vibration of the cable was investigated experimentally as well (Cosentino *et al.* 2003, Li *et al.* 2010, Jing *et al.* 2015, 2017). The other approach is to attach an artificial rivulet model on the surface of the cable model (Yamaguchi 1990, Gu and Lu 2001, Matsumoto *et al.* 2005, Xu *et al.* 2006, Gu and Huang 2008, Du *et al.* 2013). Most of these tests were conducted to obtain the aerodynamic characteristics of the cable by measuring either wind pressures around the cable (Cosentino *et al.* 2003, Du *et al.* 2013) or wind forces on the cable (Gu and Lu 2001, Matsumoto *et al.* 2005, Xu *et al.* 2006). Quantitative analyses of aerodynamic forces of

*Corresponding author, Associate Professor
E-mail: dxq@shu.edu.cn

the upper rivulet are rare because of the extreme small geometrical size of the rivulet. On an enlarged cable model, Du *et al.* (2013) obtained aerodynamic characteristics of the upper rivulet in tests, such as the distributions of wind pressures and aerodynamic forces acting on the upper rivulet.

Based on the aerodynamic information obtained in wind tunnel tests, researchers have developed various theoretical models to study the nature of RWIV analytically (Yamaguchi 1990, Geurts and Staaldin 1999, Gu and Lu 2001, Xu and Wang 2003, Peil and Dreyer 2007, Gu *et al.* 2009, Li *et al.* 2013). These theoretical studies highly depend on the experimental studies to provide essential data of aerodynamic forces acting on the cable and the rivulet to develop rational models for RWIV using the quasi-steady assumption. According to the authors' knowledge, none of these theoretical models have considered the influence of wind-induced skin frictions of the upper rivulet. The skin frictions acting on the upper rivulet may be necessary for the presence of the upper rivulet as it is protruded on the surface of the cable.

More recently, numerical simulations based on the computational fluid dynamics have been adopted to investigate the formation mechanism of the upper rivulet (Lemaitre *et al.* 2007, Taylor and Robertson 2011, Bi *et al.* 2013, Wang *et al.* 2016). Lemaitre *et al.* (2007) have developed a two-dimensional (2-D) model within the lubrication theory to describe the evolution of the rivulet subjected to gravity, surface tension, wind and motion of the cylinder. Bi *et al.* (2013) and Wang *et al.* (2016) build a 2-D coupled model based on the combination of lubrication theory and vibration theory of the single-model system to analyze the relationships between rivulet movements and cable vibration. In these models, to obtain accurate wind loading acting on the rivulet is vital to simulate the formation process and the oscillation of the rivulet. Lemaitre *et al.* (2007) assumed that the wind loading was equal to those on a dry cable, while Bi *et al.* (2013) and Wang *et al.* (2016) obtained wind loading by solving 2-D steady Navier-Stokes equations using $k-\omega$ SST transitional model. It is well known that flow around a circular cylinder in subcritical Reynolds number is characterized by complex unsteady phenomena such as flow separation, transition, and formation and shedding of vortices. The presence of upper rivulet on the circular cylinder will influence the separation and development of the shear layer, and may trigger an early transition and reattachment of the separated shear layer. Thus, the rivulet induces a pronounced effect on the mean and fluctuation aerodynamic forces on the circular cylinder. These phenomena cannot be captured precisely using steady RANS turbulent models, and more accurate CFD methods are needed to predict aerodynamic characteristics of the upper rivulet.

In this study, large eddy simulation (LES) method is used to investigate flow around and aerodynamics of a circular cylinder with an upper rivulet in a uniform flow at a high Reynolds number of 140,000. Firstly, aerodynamic characteristics of both the circular cylinder and the rivulet, such as mean aerodynamic force coefficients, pressure coefficients, and skin friction coefficients, are presented for

the rivulet at various positions. Secondly, static force analysis of the upper rivulet under the influence of the self-weight, wind-induced pressures and frictions is conducted to determine the conditions for the appearance of the rivulet on the upper side of a circular cylinder. Thirdly, the relationships between the instantaneous flow field, the pressure field, and the aerodynamic forces are investigated with the upper rivulet located at three typical positions. Finally, the dynamic characteristics of the separation bubble are investigated to shed light on the reason for the occurrence of non-zero mean lifts and RWIV of the stay cable. The present research is helpful to clarify the formation mechanism of the upper rivulet and to establish more refined theoretical models of RWIV using the aerodynamic forces obtained.

2. Numerical method and computational model

2.1 Numerical method

LES method is adopted in the present study because it can explicitly resolve transient features of the flow field such as separation and reattachment and vortex shedding, which is vital to simulate the flow correctly around a circular cylinder with an upper rivulet. The governing equations employed in LES approach are obtained by filtering the classical time-dependent filtered Navier-Stokes equations as follows

$$\frac{\partial \rho \bar{u}_i}{\partial x_i} = 0 \quad (1)$$

$$\frac{\partial}{\partial t}(\rho \bar{u}_i) + \frac{\partial}{\partial x_j}(\rho \bar{u}_i \bar{u}_j) = -\frac{\partial \bar{p}}{\partial x_i} + \frac{\partial}{\partial x_j}(\mu \frac{\partial \bar{u}_i}{\partial x_j}) - \frac{\partial \tau_{ij}}{\partial x_j} \quad (2)$$

where, \bar{u}_i and \bar{p} are the filtered velocity and pressure, ρ is the fluid density, μ is the dynamic viscosity and τ_{ij} is subgrid scale (SGS) stress tensor defined by

$$\tau_{ij} = \overline{\rho u_i u_j} - \rho \bar{u}_i \bar{u}_j \quad (3)$$

According to the Boussinesq's hypothesis, the sub-grid stress tensor is expressed as

$$\tau_{ij} - \frac{1}{3} \tau_{kk} \delta_{ij} = -2\mu_t \bar{S}_{ij} \quad (4)$$

where μ_t is the subgrid-scale turbulent viscosity and \bar{S}_{ij} is the rate-of-strain tensor for the resolved scale defined by

$$\bar{S}_{ij} = \frac{1}{2} \left(\frac{\partial \bar{u}_i}{\partial x_j} + \frac{\partial \bar{u}_j}{\partial x_i} \right) \quad (5)$$

In this study, Smagorinsky-Lilly model (Smagorinsky 1963) is adopted to model the subgrid-scale turbulent viscosity

$$\mu_t = \rho L_s^2 |\bar{S}| \quad (6)$$

Where $|\bar{S}| = \sqrt{2\bar{S}_{ij}\bar{S}_{ij}}$, and L_s is the mixing length for subgrid-scales and defined as

$$L_s = \min(\kappa d, C_s \Delta) \quad (7)$$

Where κ is the von Karman constant, d is the distance to the closest wall, Δ is the volume of a computational cell, and C_s is the Smagorinsky constant and is set to 0.1 in this study.

The Finite volume method is used to resolve the flow field numerically. Commercial CFD solver, Ansys Fluent, is adopted to conduct the simulation. The bounded central differencing scheme is used for the convection discretization and the second order implicit scheme for the transient formulation. The pressure-velocity coupling is achieved using the SIMPLEC algorithm.

2.2 Computational model

The present numerical model is based on several assumptions and simplifications to focus on the most critical scenarios. A static non-yawed circular cylinder with an upper artificial rivulet is used in the simulation. That means that the effects of inclination of the stay cable have not been considered in the present model. Furthermore, since previous studies show that the lower rivulet has little effect on the RWIV, only the upper rivulet is considered in the model, and the influence of the lower rivulet has been neglected. Finally, we assume that the shape and size of the upper rivulet do not change with the position of the rivulet. It should be mentioned that the aerodynamics of the cable and rivulet is related to the shape of the rivulet. And during the occurrence of the RWIV, the shape of rivulet is changing as it oscillates circumferentially on the cable surface.

Fig. 1 illustrates the schematic of a cable model with an upper rivulet and the detailed geometric information of the upper rivulet. The position of the rivulet is defined by the angle between the rivulet and the stagnation point, denoted by θ_u . The increment interval of θ_u is 10° for the upper rivulet position in the range from 0° to 50° and 80° to 100° , and 5° for 50° to 70° , and 2° at around 60° . Totally 18 positions are calculated in this study. The surface position on the cylinder is defined as θ_{cyl} , which is the angle between the surface position and the stagnation point. The shape and size of the upper rivulet are similar to the one used in wind tunnel tests by Du *et al.* (2013). The rivulet has an arc surface with a diameter of $d = 0.065D$ (where D is the diameter of the cable model). The width and height of the arc surface are around $0.1D$ and $0.024D$ respectively. Furthermore, because RWIV occurs mainly in the Reynolds number range of 50,000 to 200,000 (Matsumoto *et al.* 1990), present simulations are carried out at Reynolds number of 140,000 based on the diameter of the cable model, D , and the free stream velocity U_o . The free stream velocity is set as $U_o = 12.68$ m/s, while the diameter of the cylinder is $D = 0.16$ m.

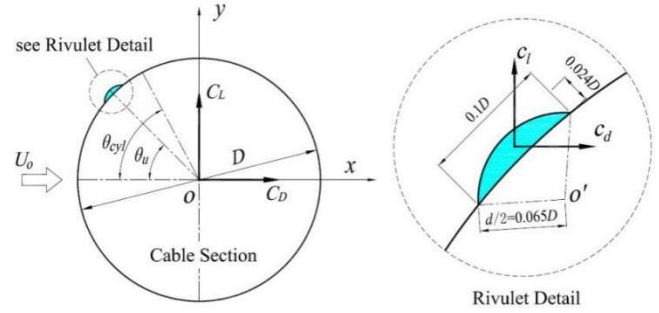


Fig. 1 Schematic diagram of a cable model with an upper rivulet

2.3 Computational domain and mesh

The computational domain and the boundary conditions are shown in Fig. 2. The size of the computational domain is adopted by reference to those of Cao and Tamura (2015); Behara and Mittal (2011). The inlet has been set a sufficient distance ($8D$) away from the center of the cylinder to prevent the inlet boundary condition from being disturbed by the unsteady flow around the cylinder. The lateral width of the domain is $16D$, which results in a blockage ratio of 6.25%. According to the study on the effects of tunnel blockage by West and Apelt (1982), if the blockage is less than 6%, the mean drag coefficient of a circular cylinder varies only slightly with blockage, and the Strouhal number is independent of the blockage ratio. Present blockage ratio is close to this critical blockage. The outlet has been set a distance ($20D$) away from the center of the cylinder to ensure a fully developed wake. A relatively short span ($L_z = 1D$) is chosen because of limited computational resources. Both the surfaces of the cylinder and the rivulet are considered as smooth surfaces. The no-slip wall boundary is specified on the surfaces of the cylinder and the rivulet, and the velocity-inlet boundary condition is set to $u = U_o$, $v = w = 0$. The zero velocity-gradient condition is used as the outflow boundary. Symmetry conditions are given for upper and lower boundaries. Periodic boundary conditions are employed at the span-wise boundaries to simulate an infinitely long cylinder, which implies that the flow can come into or out of the computational domain through the span-wise boundaries.

Structured grids are adopted to discretize the spatial computational domain. Fig. 3 is illustrated the grid in the x - y plane, with a close-up view mesh near the cylinder and the upper rivulet. A body-fitted grid layer is generated at the wall where the minimum cell height normal to the cylinder wall is $4 \times 10^{-4}D$, and the growth ratio of the cell height in the radial direction is 1.05 near the cylinder. The value of y^+ on the surface of the cylinder and the rivulet is less than 1. In the span-wise direction, the grid cells are uniformly distributed with an interval of $0.1D$. At the circumference of the model, there are 400 nodes on the circular cylinder and 30 nodes on the rivulet. The total grid cells are 0.98 million. The non-dimensional time step ($\Delta t^* = \Delta t U_o / D$) is set equal to 0.001 to ensure the CFL number less than 1 in the shear

Table 1 Parameters of cable and rivulet

Case	Re	L_z	Circumferential grid	C_D	St
Case1	1.4×10^5	$1D$	256	1.113	0.189
Case2	1.4×10^5	$1D$	320	1.289	0.192
Case3	1.4×10^5	$1D$	400	1.323	0.191
Case4	1.4×10^5	$2D$	400	1.258	0.190
Case5	1.4×10^5	$4D$	400	1.194	0.194
Nishuimura (2001)	6.1×10^4	\	\	1.224	0.202
Cantwell & Coles (1983)	1.4×10^5	\	\	1.237	0.179
Schewe (1983)	1.4×10^5	\	\	1.20	0.20

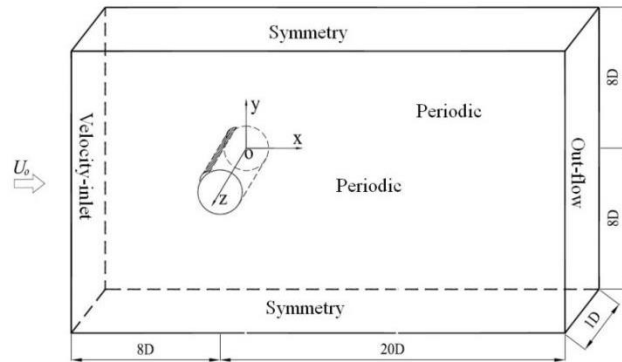
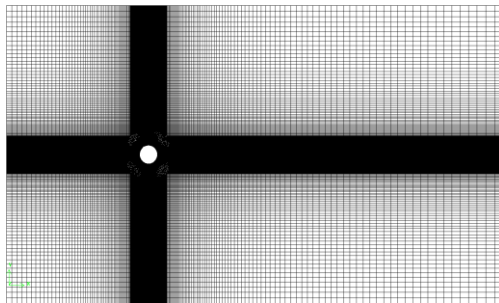
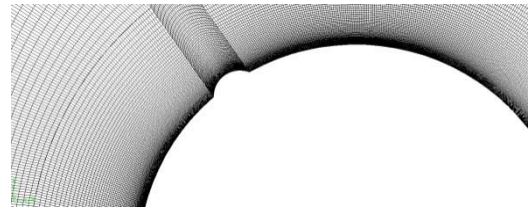


Fig. 2 Computational domain and boundary conditions



(a) The whole domain



(b) Near the cylinder

Fig. 3 The computational grid in the x - y plane

layer regions and the near wake of the circular cylinder. The present time step is also similar to those adopted by Cao and Tamura (2015) and Behara and Mittal (2011). The statistics of aerodynamic characteristics are computed for a time span of more than 20 vortex-shedding cycles. In order to get steady statistic results, the flow passes through the domain about 4 times before activating the averaging process. The statistic results are calculated for about 4.5 times of flow-through time.

Mesh dependency and model validation has been conducted first on a plain circular cylinder without rivulet at $Re = 140000$. The influences of the span-wise length and the circumferential grid on the aerodynamic characteristics of the cylinder are investigated. The computational results have been listed in Table 1 and compare with those

obtained by wind tunnel tests in literature. We adopt a numerical model with similar parameters to Case3 to simulate the flow around a circular cylinder with a rivulet.

It can be seen that both the mean drag coefficient and Strouhal number is getting closer when the grid number increases from 256 to 400. Also, the mean drag coefficients are reduced from 1.323 to 1.194 as the aspect ratio increases from $L_z/D = 1$ to 4, which is consistent with the results by Cao and Tamura (2015). Moreover, the Strouhal number is around 0.19 for all the six present cases, which is close to those obtained in wind tunnel tests. Due to the relatively small span-wise length used in present study, the present mean drag coefficient of 1.323 which is about an overestimate of 7% to 10% in comparison with that of Cantwell & Coles (1983) and Schewe (1983) respectively.

2.4 Definitions of aerodynamic coefficients

Non-dimensional pressure coefficient and friction coefficient on the surface of the circular cylinder and the rivulet can be expressed respectively by

$$c_p = \frac{p - p_o}{\frac{1}{2}\rho U_o^2} \quad (8)$$

$$c_f = \frac{\tau_u}{\frac{1}{2}\rho U_o^2} \quad (9)$$

where ρ is the air density; p is the pressure at the point where the pressure coefficient is being evaluated; p_o is the pressure in the free stream; τ_u is the surface shear stress and defined as

$$\tau_u = \mu \frac{\partial V}{\partial n} \quad (10)$$

where μ is the viscosity coefficient, $\partial V/\partial n$ is the normal velocity gradient at the surface of the models.

The aerodynamic force coefficients of the circular cylinder are defined as

$$C_D = \frac{F_D}{\frac{1}{2}\rho U_o^2 D} \quad (11)$$

$$C_L = \frac{F_L}{\frac{1}{2}\rho U_o^2 D} \quad (12)$$

where C_D and C_L are aerodynamic coefficients of the circular cylinder in x and y directions respectively, and their directions are defined in Fig. 1; F_D and F_L are the aerodynamic forces on the cylinder of per unit length, which can be obtained through integrating the wind pressures over the whole circumference of the cylinder excluding the contribution of pressures on the rivulet.

The aerodynamic force coefficients of the rivulet as shown in Fig. 1 are defined as

$$c_d = \frac{f_d}{\frac{1}{2}\rho U_o^2 d} \quad (13)$$

$$c_l = \frac{f_l}{\frac{1}{2}\rho U_o^2 d} \quad (14)$$

where c_d and c_l are aerodynamic coefficients of the rivulet in x and y directions respectively. d is the reference length of the rivulet and is the arc diameter of the rivulet model in this paper, i.e., $d = 0.13D$. f_d and f_l are the aerodynamic forces per unit length acting on the rivulet obtained through integrating the wind pressures over the rivulet in x and y

directions.

The drag coefficient of a circular cylinder consists of two parts, the friction drag coefficient, and pressure drag coefficient. However, the friction one is negligible comparing to the pressure one when the Reynolds number greater than 10^4 (Zdravkovich 1990). Therefore, in the following section, only the contribution of the pressure coefficient is considered to calculate the aerodynamic force coefficients of the circular cylinder. For the upper rivulet, on the other hand, the contribution of the friction coefficient may not be neglected because the rivulet protrudes on the surface of the cylinder and may suffer relatively large friction forces. Furthermore, the friction force can balance parts of the self-weight of the rivulet and prevent the rivulet from sliding down the cable, which is essential for the appearance of a rivulet on the upper-side of a stay cable. Therefore, it is considered the influence of both pressures and skin frictions to calculate the drag coefficients and the lift coefficient of the rivulet in this paper. The total drag coefficient c_d and lift coefficient c_l of the upper rivulet whose directions are shown in Fig. 1 are defined as

$$c_d = c_d^p + c_d^f \quad (15)$$

$$c_l = c_l^p + c_l^f \quad (16)$$

where the superscript “ p ” and “ f ” denotes the contribution from pressures and frictions respectively.

3. Results and discussion

3.1 Aerodynamics of a circular cylinder with an upper rivulet

3.1.1 Mean aerodynamic coefficients

Fig. 4 illustrates the mean aerodynamic force coefficients of the circular cylinder as a function of the rivulet position θ_u . Three results obtained in wind tunnel tests (Gu and Lu 2001, Matsumoto *et al.* 2005, Du *et al.* 2013) are listed in the figure as well. It can be seen from the figure that the curve profile of aerodynamic force coefficient in present simulation is similar to those of literature. Both drag and lift coefficients show considerable variations as the upper rivulet located at different positions. Specifically, the mean lift coefficients of present study experience three distinct stages, zero-lift stage, positive-lift stage and negative-lift stage when θ_u is located within three ranges: 0° to 50° , 50° to 65° and 65° to 90° . As for the first stage, i.e., θ_u between 0° and 50° , the upper rivulet has little influence on the lift and the mean lift coefficients keep at zero steadily. At the second stage, i.e., θ_u between 50° and 65° , the large mean lift forces appear in the positive direction. At the third stage, the lift force coefficients decrease dramatically from positive to negative as θ_u increasing from 65° to 80° , with the drag force coefficients increase considerably. Those lift coefficients obtained by

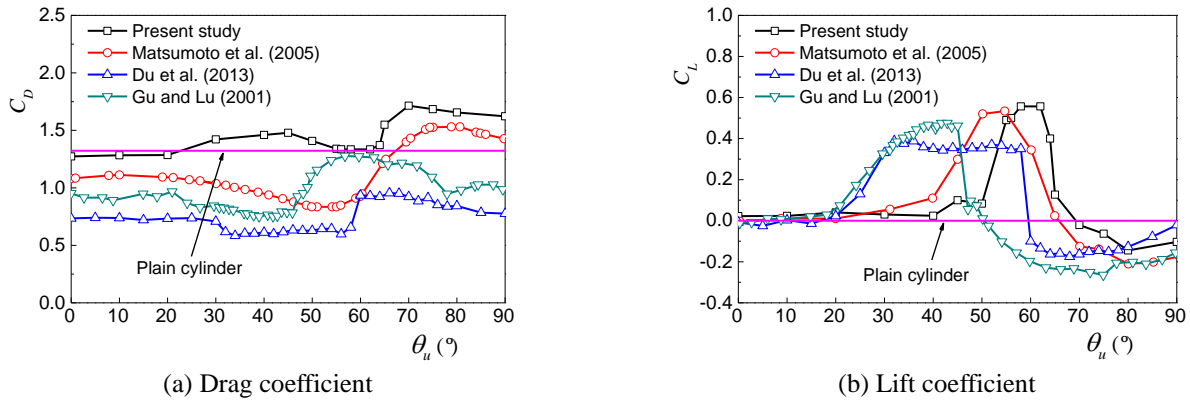


Fig. 4 Mean aerodynamic force coefficients of the circular cylinder

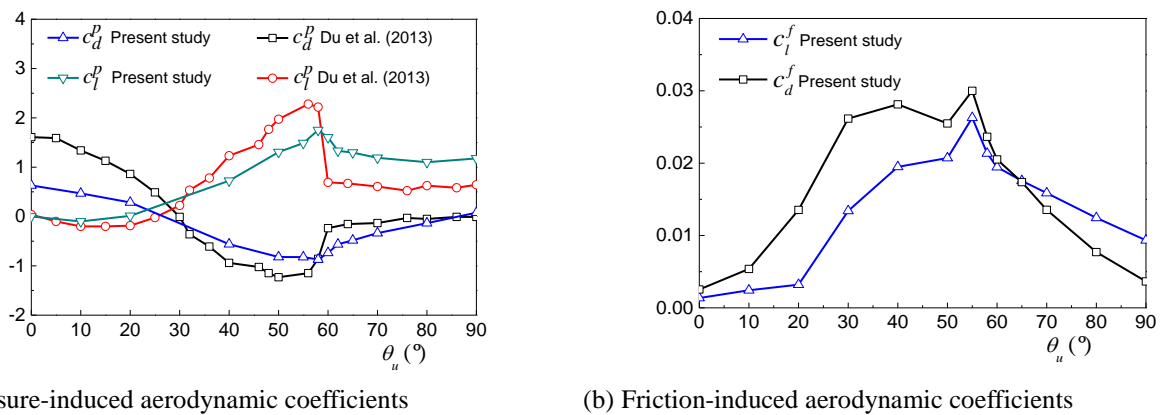


Fig. 5 Mean aerodynamic force coefficients of the upper rivulet

wind tunnel tests also experience similar three stages. As for the mean drag coefficient, see Fig. 4(a), the present results are generally larger than those of literature. As mentioned above, the overestimated mean drag coefficients may be due to the relatively small span-wise length of the model.

It should be noted that, similar to a plain circular cylinder, the aerodynamic characteristics of the circular cylinder with the rivulet is highly sensitive to many factors, such as the free-stream turbulence, Reynolds number, the surface roughness, etc. Matsumoto *et al.* (2005) pointed out that the shape and size of the rivulet also have significant influences on the aerodynamics of a circular cylinder. Matsumoto *et al.* (2005) used a rectangular rivulet, while Gu and Lu (2001) adopted a half ellipse one. As described above, we choose a circular segment rivulet which is similar to the one used by Du *et al.* (2013). However, the intensity of the free-stream turbulence is different between the present simulation and wind tunnel tests of Du *et al.*, with 0% in this study and about 2% in the tests. Lifted turbulence makes the reattachment of shear layer happen at a lower rivulet position, resulting in a non-zero mean lift begun at around $\theta_u = 30^\circ$ for the lift coefficient of Du *et al.* Thus, present lift coefficients for $\theta_u = 30^\circ$ and 80° are different those in literature as shown in Fig. 4(b). Even the three experimental results show apparent discrepancies, which

were obtained under different test conditions.

Fig. 5 shows the mean aerodynamic force coefficients of the upper rivulet as a function of the rivulet position θ_u . In order to examine the contribution of the skin friction, the aerodynamic force coefficients are divided into two parts, pressure-induced one and friction-induced one. It can be seen from Fig. 5(a) that the pressure-induced force coefficients of the present simulation study are similar to those of the results obtained in wind tunnel tests (Du *et al.* 2013). When θ_u between 30° and 60° , both the drag and lift coefficients vary considerably with the position of the rivulet. It will be seen in the next section that the rivulet locates mainly in the suction zone and suffers negative pressures when $\theta_u = 30^\circ$ - 60° , which makes the rivulet subject a negative drag and a positive lift. While for the friction-induced force coefficients, see Fig. 5(b), both the drag and lift coefficients are positive and keep at high levels when $\theta_u = 30^\circ$ - 60° , which is helpful for the rivulet standing on the upper side of the cable. It will be discussed further the contribution of friction-induced forces to the appearance of the upper rivulet.

3.1.2 Mean pressure coefficients

Fig. 6 presents the pressure coefficient distributions of the circular cylinder and the rivulet for six typical rivulet

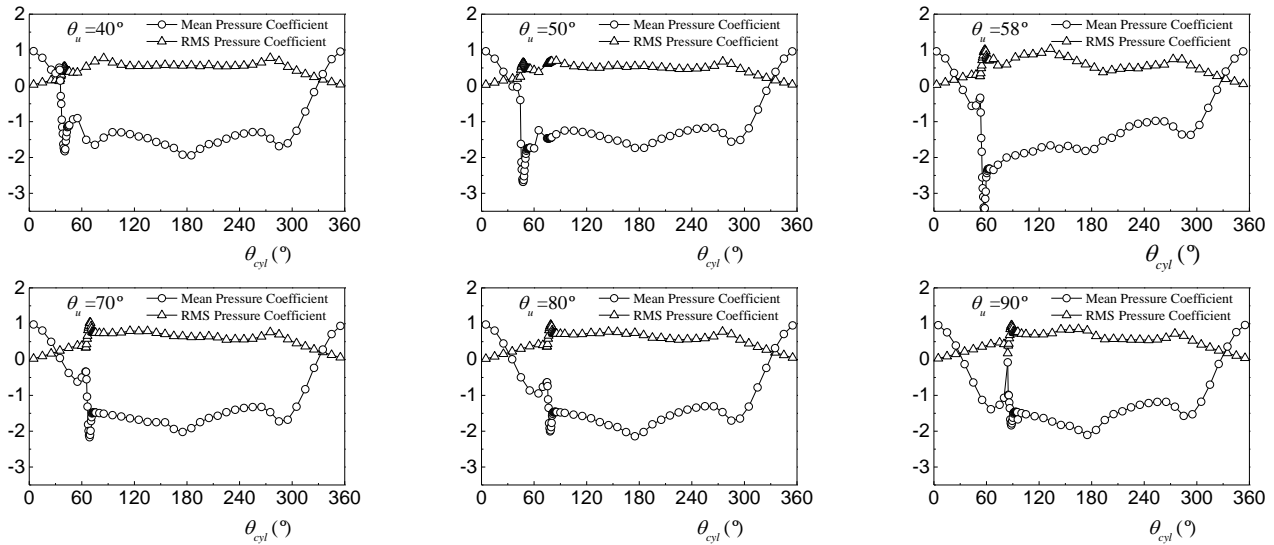


Fig. 6 Mean and RMS pressure coefficients of the circular cylinder with rivulet

positions, $\theta_u = 40^\circ, 50^\circ, 58^\circ, 70^\circ, 80^\circ, 90^\circ$, within three stages of mean lift coefficients.

When $\theta_u = 40^\circ$, see Fig. 6, the mean pressure distribution are nearly symmetrical between the upper-side of the cylinder and the lower-side except for a small region near the rivulet, which indicates the upper rivulet have little influence on the aerodynamics of the cylinder. As θ_u increasing to 58° , the mean pressure coefficients on the upper rivulet decrease significantly, and the negative pressure coefficient on the rivulet reaches up to -3.5 . The asymmetrical pressure distribution of the cylinder results in a non-zero positive mean lift as shown in Fig. 4(b). It will be seen in the following section that the non-zero mean lifts are the result of a separation-reattachment bubble formed on the upside of the cylinder. The shear layer separated from the upper rivulet can reattach at the surface of the cylinder behind the rivulet when the rivulet is located between 50° - 65° . When $\theta_u = 70^\circ$ and 80° , the separation-reattachment bubble disappears. However, the upper rivulet still disturbs the separation of the upside shear layer, which results in another kind of asymmetrical pressure distribution and a non-zero negative lift. With θ_u reaching to 90° , it can be seen from Fig. 6 that although the upper rivulet is located behind the separation point, it still has some influences on the pressure of the cylinder.

3.1.3 Mean friction coefficients

Before investigating the friction distribution around the circular cylinder with rivulet, the friction of a circular cylinder without rivulet (a plain circular cylinder) are examined first. Fig. 7 shows the mean friction coefficients around the plain cylinder at Reynolds number of 1.4×10^5 . The results from two kinds of literature are listed as well to compare, one by wind tunnel tests at $Re = 10^5$ (Achenbach 1968) and the other by LES at $Re = 3900$ (Breuer 1998). It can be seen that the present results agree well with those of Achenbach (1968) with the maximum friction coefficient occurring at around $\theta_{cyl} = 60^\circ$. However, the present results differ considerably from those of Breuer (1998), which may

be due to the significant difference of Reynolds number. According to Achenbach (1968), the friction distribution of a circular cylinder is dependent on the Reynolds number, the surface roughness, and the turbulence level.

Fig. 8 illustrates the mean friction coefficient distributions around the circular cylinder with and without rivulet. The results of six rivulet positions are selected to compare with the plain cylinder. It can be seen that the upper rivulet has profound impacts on the friction around the cylinder especially when the rivulet is located at $\theta_u = 58^\circ, 70^\circ, 80^\circ$, *i.e.*, near the separation point of the plain cylinder. When $\theta_u = 20^\circ$ and 40° , the upper rivulet locally affects the friction of the cylinder near the rivulet. As for $\theta_u = 90^\circ$, the friction coefficients of the cylinder with rivulet are similar to those of the plain cylinder except on the rivulet. The peak friction coefficient on the rivulet reaches the maximum value when $\theta_u = 58^\circ$, which is much higher than that of the plain cylinder. Furthermore, the peak friction coefficient on the rivulet grows steadily as θ_u increasing from 20° to 58° , but decreases as θ_u increasing further beyond 58° .

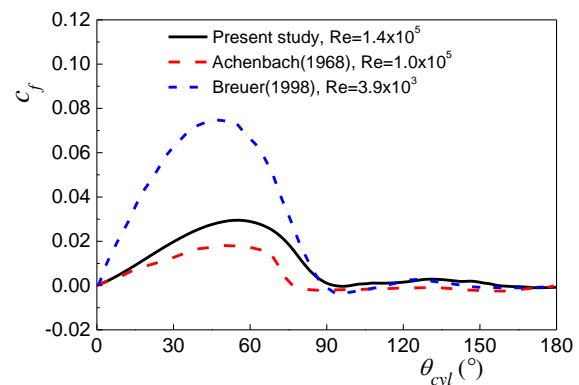


Fig. 7 Mean friction coefficients of a plain circular cylinder (without rivulet)

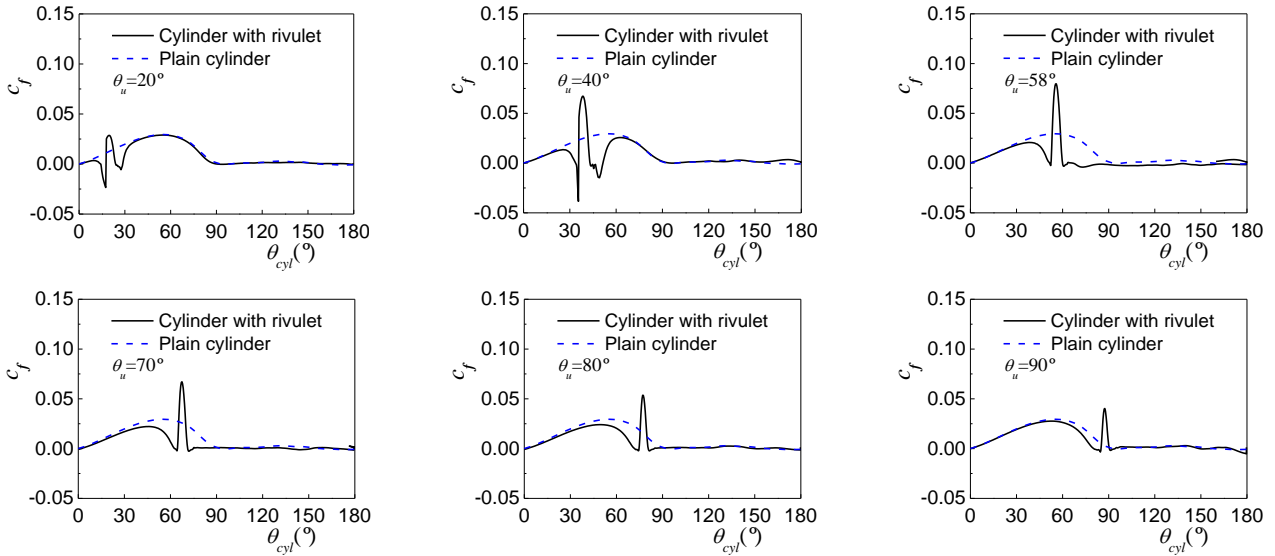


Fig. 8 Mean friction coefficients of the circular cylinder with rivulet

3.2 Static force analysis of upper rivulet

It has been confirmed in the past study that the appearance of the upper rivulet on the stay cable is key to the occurrence of the RWIV. However, the reasons why the rivulet can stand steadily on the upside of the cable have not been clarified yet. This section will investigate the role of the pressure and friction on the upper rivulet played in the appearance of the rivulet.

Considering the situation that the upper rivulet has appeared on the stay cable but the cable and the rivulet have not begun to vibrate, the assumption that the rivulet and the cable are static is adopted here. Therefore, the friction force in the interface between the cable and rivulet is not considered. Besides, we have not considered the influence of the rivulet's shape on the aerodynamic forces as mentioned before. Fig. 9 presents the scheme of static force analysis of the upper rivulet. Fig. 9(a) shows the aerodynamic forces acting on the upper rivulet, pressures and skin frictions, while Fig. 9(b) illustrates direction definitions of aerodynamic force coefficients of the rivulet induced by pressures and frictions. The drag and lift force coefficients of the upper rivulet defined by Eqs. (13)-(16) can be resolved to the components in the normal (n) and tangential (t) directions using following equations

$$c_n = -c_d \cos \theta_u + c_l \sin \theta_u \quad (17)$$

$$c_t = c_d \sin \theta_u + c_l \cos \theta_u \quad (18)$$

Fig. 9(c) illustrates the loads acting on the static upper rivulet. The rivulet is subjected to the following forces: pressure-induced aerodynamic forces (f_n^p, f_t^p), friction-induced aerodynamic forces (f_n^f, f_t^f), the gravity of the rivulet ($mg \cos \alpha$, here α is the inclined angle of a stay cable, i.e., the angle between the cable axis and the horizontal), normal force of the cable surface (N) and rivulet-cable

surface tensions at upper and lower side of the rivulet (f_u^{st}, f_l^s). In the present analysis, the surface tensions are neglected as they are hard to be determined. Therefore, if the upper rivulet can rest steadily on the upside of the cable, the forces exerted on the rivulet must balance to zero in the tangential direction.

$$f_t^p + f_t^f - mg \cos \alpha \cos \theta_u = 0 \quad (19)$$

Fig. 10 shows the tangential aerodynamic force coefficients of the upper rivulet caused by pressures and frictions respectively. It can be seen that both of the force coefficients are positive at nearly all of the rivulet positions, which is helpful for the rivulet to stand on the upside of the cable by resisting the self-weight of the rivulet. The pressure-induced force coefficient reaches the highest value at the rivulet position $\theta_u = 50^\circ$, while the maximum value of the friction-induced coefficient occurring at $\theta_u = 55^\circ$. After that, both the force coefficients decrease with the increase of the rivulet position. Furthermore, the magnitude of the friction-induced coefficient is around 15%-20% of the pressure-induced coefficient, which indicates that the contribution of the aerodynamic friction to the appearance of the upper rivulet cannot be neglected.

To qualitatively investigate the relationship between the self-weight of the upper rivulet, wind-induced pressure, and friction, static force analysis of an upper rivulet is conducted based on the parameters listed in Table 2. These parameters are adopted by reference to those used in the wind tunnel tests of Gu and Du (2005). It has been found that the cable model with a diameter of 120mm is prone to RWIV under the conditions of inclined angle of about 30° and the wind speed ranging from 8-9 m/s (Gu and Du 2005). The shape and size of the upper rivulet are shown in Fig. 1 which are similar to those used by Du *et al.* (2013), and the mass of the upper rivulet are calculated according to these geometrical parameters.

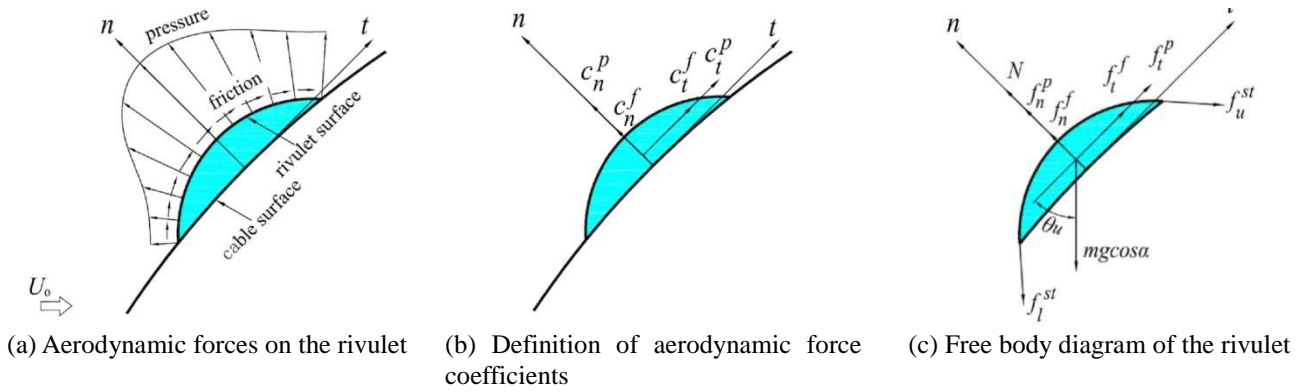


Fig. 9 Scheme of force analysis of a static upper rivulet

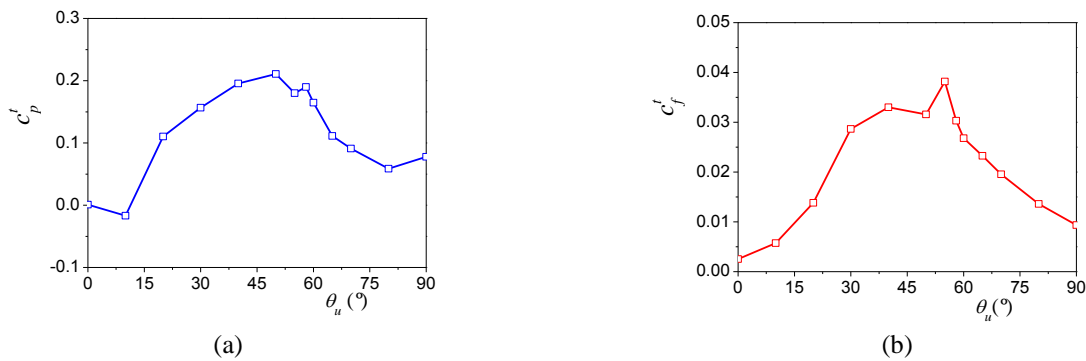


Fig. 10 Tangential aerodynamic force coefficients induced by (a) pressures and (b) frictions

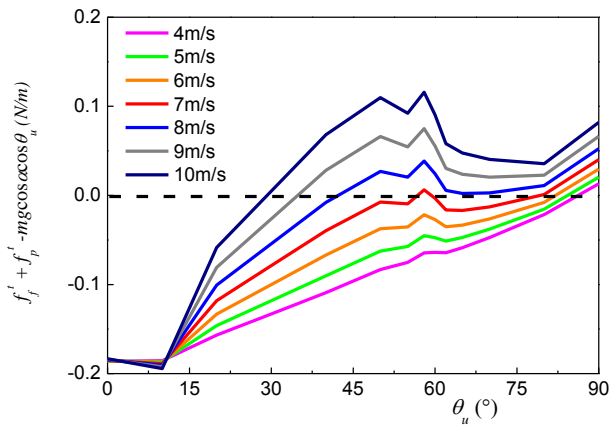


Fig. 11 Resultant mean aerodynamic forces and self-weight of the rivulet in the tangential direction

Table 2 Parameters of cable and rivulet

Parameters	Values
Diameter of the stay cable, D (mm)	120
Inclined angle of the stay cable, α	30°
Mass of the upper rivulet, m (kg/m)	0.022
Wind speed, U_o (m/s)	6-10

Fig. 11 illustrates the resultant forces on the upper rivulet in the tangential direction, $f_t^p + f_t^f - mg \cos \alpha \cos \theta_u$, which are calculated using the data from Table 2 and Fig. 10. It can be seen from the figure that when the wind speed is relatively low, saying less than 6m/s, the resultant forces are mostly negative except when the rivulet located in the range near $\theta_u = 90^\circ$. However, when a rivulet forms at around $\theta_u = 90^\circ$, it has little influence on the aerodynamics of stay cable, which can be seen from the Fig. 4. Therefore, when the wind speed is too low, the rivulet is hard to exist at the upside of the cable and the RWIV of the stay cable cannot happen. As the wind speed increases to 8 m/s, the resultant forces can be positive when θ_u at around $40-70^\circ$, which indicates that the aerodynamic forces can resist the self-weight of the rivulet and the rivulet can stand at the upside of the cable. It can be seen the Fig. 4 that the aerodynamics of a stay cable change significantly as the rivulet position θ_u located between $40-70^\circ$, which may result in RWIV of the stay cable. When the wind speed increases further, the range where the resultant forces are positive is getting wider. Nevertheless, it can be anticipated that excessive wind speed will drive the rivulet moving leeward and the rivulet will either be blown off or move to the region where the rivulet has little influence on the aerodynamics of stay cable. Therefore, the RWIV cannot happen at excessive wind speeds either. It can be concluded that the rivulet position is sensitive to the wind speed and

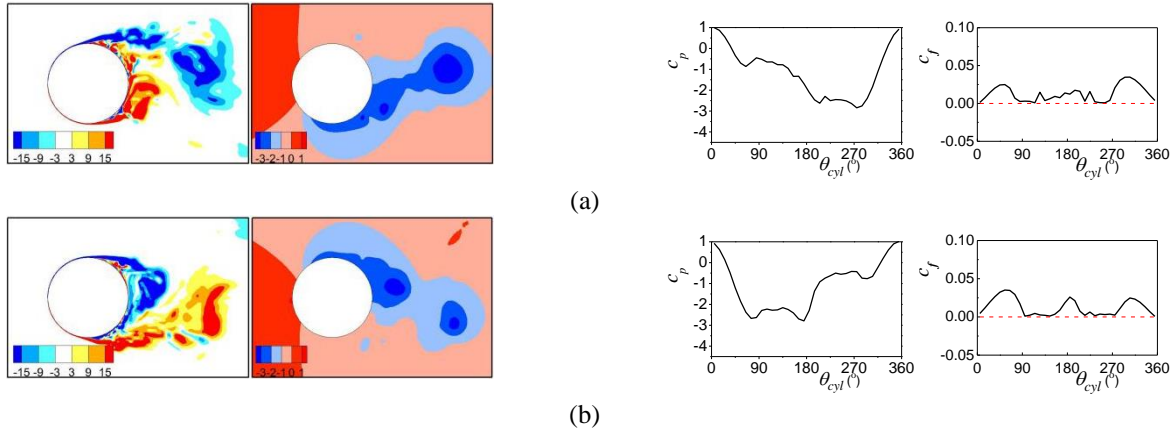


Fig. 12 Instantaneous span-wise vorticity, pressure field, and pressure coefficient and friction coefficient distribution for the plain cylinder at the moments of (a) minimum lift (T1) and (b) maximum lift (T2)

the RWIV can only occur within a limited range of wind speed. The phenomenon is consistent with those observed in field measurements (Hikami and Shiraishi 1988, Zuo and Jones 2010) and wind tunnel tests (Matsumoto *et al.* 1995, Flamand 1995, Gu and Du 2005).

3.3 Instantaneous flow field and aerodynamic force

Typical instantaneous flow fields and aerodynamic forces of the cylinder with/without the rivulet are investigated further to understand the effect of the rivulet on flow characteristics and aerodynamics of the cylinder. Five cases are selected to study, including a plain cylinder (a cylinder without rivulet) and the cylinder with the rivulet at $\theta_u = 40^\circ, 58^\circ, 80^\circ, 100^\circ$ respectively. Figs. 12-16 illustrate instantaneous span-wise vorticities (ω_z) and pressure fields on the xy plane at moments of minimum lift (T1) and maximum lift (T2) for these cases. Moreover, instantaneous distributions of pressure coefficient (c_p) and friction coefficient (c_f) around the cylinder are shown in the figures as well.

When the rivulet located at $\theta_u = 40^\circ$, see Fig. 13, both the vorticities and pressure fields show symmetric patterns for the two moments and are almost identical to those of the plain cylinder, which indicates the rivulet has little impact on the flow field around the cylinder. From the instantaneous pressure coefficient distribution around the cylinder, it can be seen that the influences of the rivulet are limited near the rivulet only. Furthermore, from the friction coefficient distribution, one can observe negative friction coefficients just before and after the rivulet, as marked by blue arrows in the figure, which suggests that there exist two small recirculation regions at the front and rear of the rivulet.

As the rivulet located at $\theta_u = 58^\circ$, it can be seen from Fig. 14, both the vorticity and the pressure field show asymmetric patterns for the moments of T1 and T2. One can observe from the snapshot of the vorticity that the shear layer separated from the rivulet can reattach on the surface of the cylinder for both moments, which results in strong negative pressures at the region behind the rivulet as shown

in the pressure field. The pressure coefficient distributions for the moments of T1 and T2 show some similarities with minimum pressures up to -4.0 at the upside of the cylinder, which results in a substantial non-zero mean lift as shown in Fig. 4(b). As for the friction coefficient distribution, one can observe a large negative friction region at the rear of the rivulet, as marked by blue arrows in the figure, which indicates that there exists a separation bubble at the rear of the rivulet. The separation bubble is an unsteady flow phenomenon, and dynamic characteristics of the separation bubble will be discussed further in the next section. Both flow field characteristics and aerodynamics of the cylinder with a rivulet at $\theta_u = 58^\circ$ show significantly different from those of the cylinder without a rivulet.

As for the case of $\theta_u = 80^\circ$, it can be seen from Fig. 15 that the friction coefficient at the rear of the upper is positive except at the region around $\theta_{cyl} = 180^\circ$, which is caused by the large recirculation in the near wake of the cylinder. Also, the span-wise vorticities show that the upper shear layer separated from the upper rivulet does not reattach to the cylinder surface. The evidence proves that there are no separation bubbles behind the upper rivulet. However, the upper rivulet still has some impacts on the flow around and aerodynamics of the cylinder when compared with the plain cylinder. As the upper rivulet is protruding from the surface of the cylinder, the distance between the upper separated shear layer and the cylinder for the moment T2 is larger than that for the moment T1. Thus the negative pressures on the upper side of the cylinder for the moment T2 are relatively weaker than those on the lower side for the moment T1, which causes a non-zero mean lift with the direction opposite to the case of $\theta_u = 58^\circ$ as shown in Fig. 4(b).

As for the case of $\theta_u = 100^\circ$, see Fig. 16, the rivulet is located behind the separation point and does not influence the separation of the boundary layer. However, the rivulet causes some disturbance to the separated shear layer and changes slightly local pressures near the rivulet, which can be seen in the pressure field and the pressure coefficient distribution in Fig. 16(b).

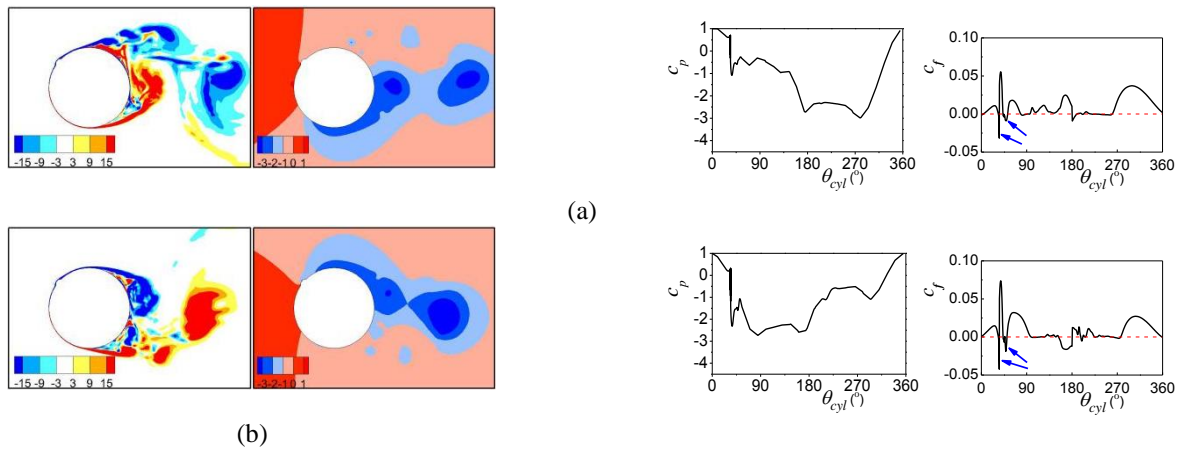


Fig. 13 Instantaneous span-wise vorticity, pressure field, and pressure coefficient and friction coefficient distribution for $\theta_u = 40^\circ$ at the moments of (a) minimum lift (T1) and (b) maximum lift (T2)

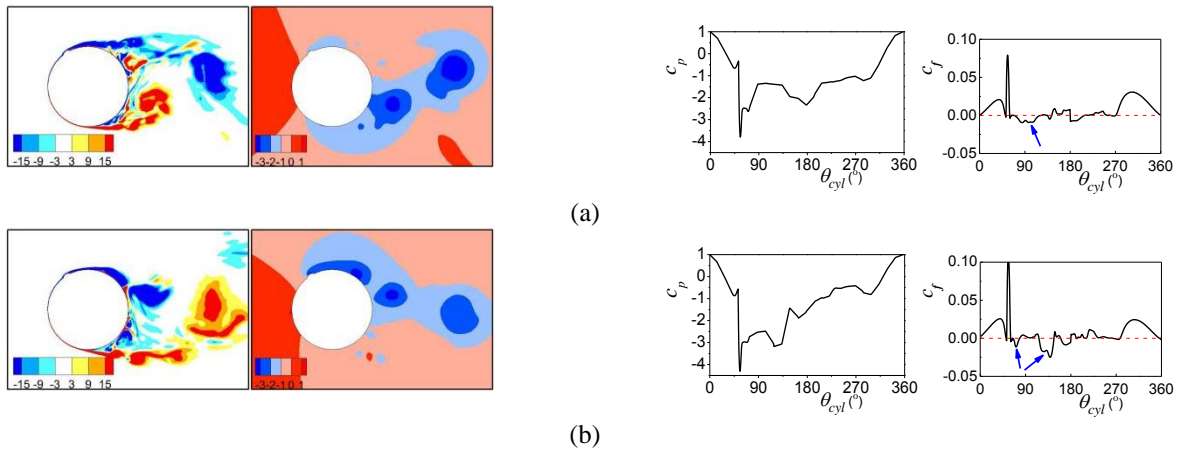


Fig. 14 Instantaneous span-wise vorticity, pressure field, and pressure coefficient and friction coefficient distribution for $\theta_u = 58^\circ$ at the moments of (a) minimum lift (T1) and (b) maximum lift (T2)

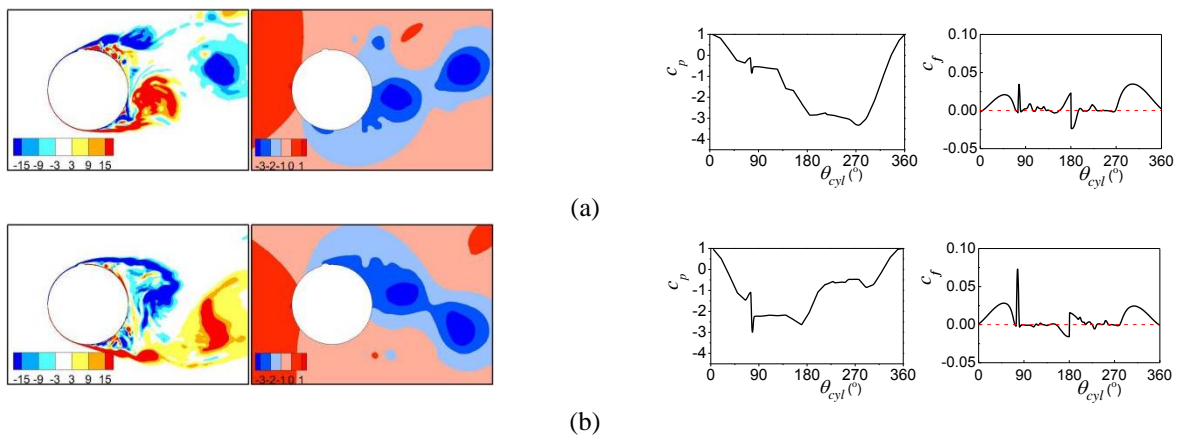


Fig. 15 Instantaneous span-wise vorticity, pressure field, and pressure coefficient and friction coefficient distribution for $\theta_u = 80^\circ$ at the moments of (a) minimum lift (T1) and (b) maximum lift (T2)

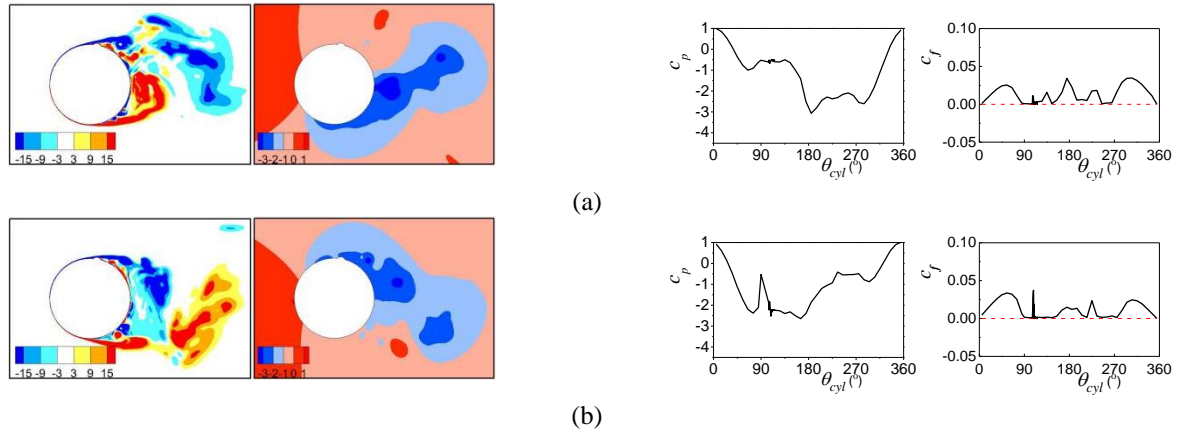


Fig. 16 Instantaneous span-wise vorticity, pressure field, and pressure coefficient and friction coefficient distribution for $\theta_u = 100^\circ$ at the moments of (a) minimum lift (T1) and (b) maximum lift (T2)

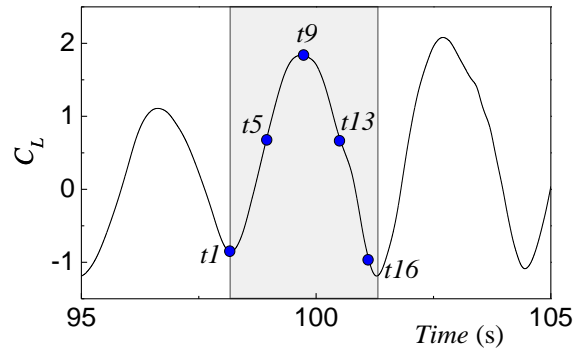


Fig. 17 Instantaneous moments in time history of lift coefficient for $\theta_u = 58^\circ$

3.4 Dynamics of the separation bubble

As discussed above, the single separation bubble appearing at the rear of the upper rivulet for $\theta_u = 50^\circ$ - 65° can cause high non-zero mean lifts on the circular cylinder, which is vital to the occurrence of rain-wind-induced vibration of stay cable. In order to investigate dynamics of the separation bubble for $\theta_u = 58^\circ$, instantaneous streamlines and pressure fields near the upper rivulet are investigated further. Fig. 18 illustrates close-up views of instantaneous streamlines and pressure fields at sixteen equally spaced intervals in a period of lift. These instantaneous moments, denoted as $t1$ - $t16$, are marked on the time history of lift coefficient in Fig. 17.

It can be seen from Fig. 18 that so-called separation bubble presented behind the upper rivulet is an unsteady flow phenomenon, which consists of a series of eddies rotating in clockwise directions and traveling along the surface of the cylinder. This phenomenon has not been observed at the lower side of the circular cylinder. These eddies change shape as they move leeward and induce strong negative pressures in the local region. At the moment of $t1$, as shown in Fig. 18, there is only one eddy on the upper surface of the cylinder, which splits into two distinct

cells at the next moment $t2$. From $t4$ to $t6$, the thickness of the eddy reduces as they propagate downstream. However, the strength of the eddy is enhanced which causes higher negative pressures locally. From $t6$ to $t9$ it seems that several eddies merge to a big eddy at the leeward of the cylinder, with the lift coefficient increasing and reaching a peak value at the moment of $t9$. The big eddy finally bursts and sheds away from the cylinder at the moment of $t10$, and the lift coefficient begins to decrease after that. It should be noted that, from $t7$ to $t14$, there exists a much steadier eddy just at the rear of the upper rivulet, which causes a high suction region near the rivulet. Up to the moment $t15$, the eddy begins to move downstream and increase in size, which is similar to the scenario of the moment $t1$.

From the above discussion, it can be concluded that laminar shear layer undergoes transition after it separating from the upper rivulet. And a series of unsteady eddies rotating in clockwise directions evolve in the shear layer.

The eddies can reattach on the surface of the cylinder as they propagate downstream. The reattachment of the separated shear layer causes strong negative pressure on the upper surface of the cylinder, which results in a high non-zero mean lift of the cylinder and potentially induces the occurrence of RWIV.

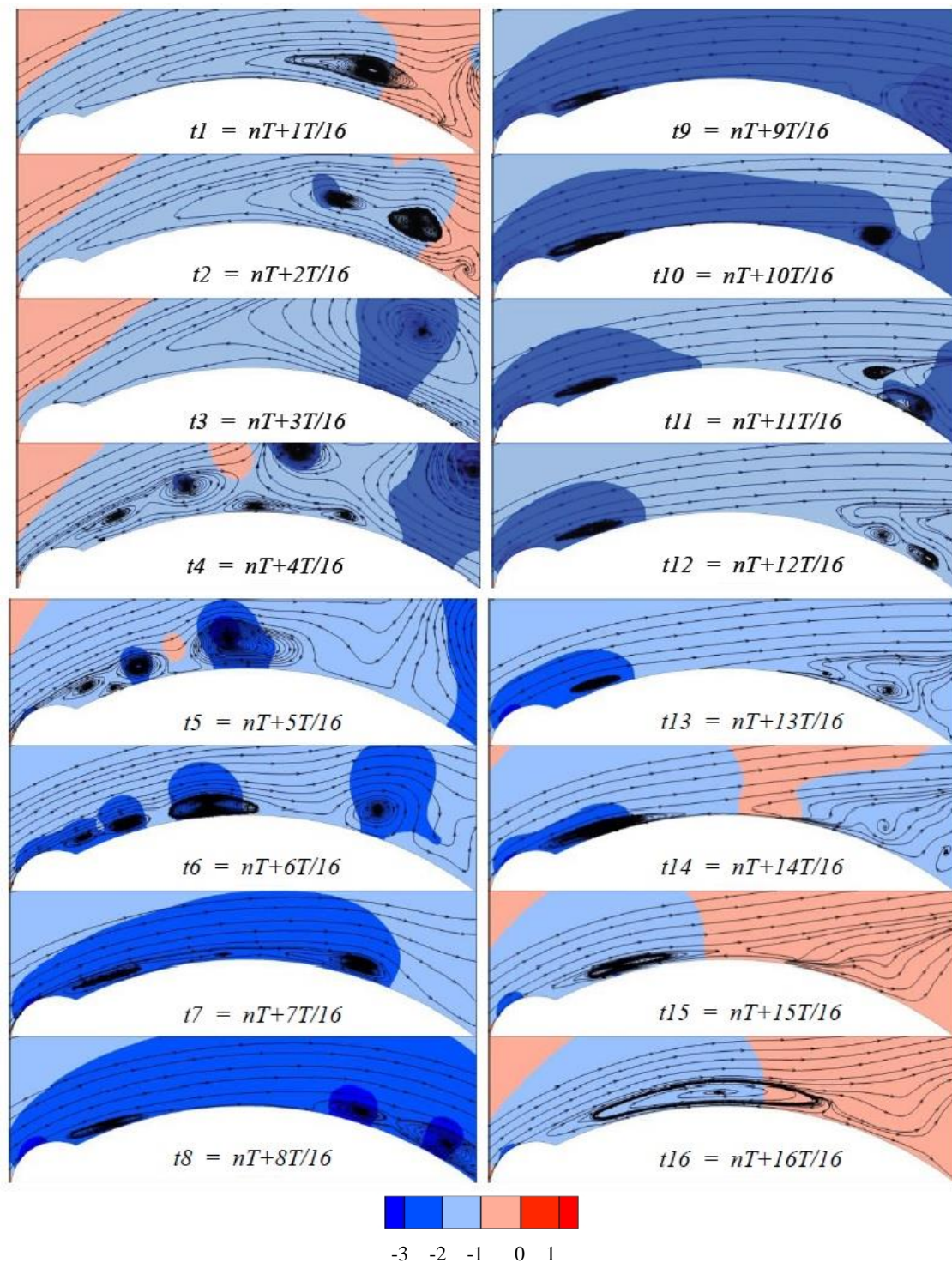


Fig. 18 Instantaneous streamline and pressure field near the upside of the cylinder during a period of lift for $\theta_u = 58^\circ$

4. Conclusions

To understand the formation mechanism of the upper rivulet and its aerodynamic effects on the stay cable, flow around a circular cylinder with an upper rivulet has been investigated using LES model at a high Reynolds number of 140,000. Following summarized main findings of this study:

- Mean aerodynamic force coefficients of the circular cylinder with the upper rivulet in present simulation are similar to those obtained in wind tunnel tests. The mean lift coefficients of the circular cylinder experience three distinct stages, zero-lift stage, positive-lift stage and negative-lift stage as the rivulet located at various positions.
- As for the tangential aerodynamic forces on the upper

rivulet, both pressure-induced and friction-induced forces are helpful for the rivulet to stand on the upside of the cable by resisting the self-weight of the rivulet. The magnitude of the friction-induced forces is around 15%-20% of the pressure-induced ones. The contribution of the aerodynamic friction to the appearance of the upper rivulet may not be neglected in modeling the movement of the rivulet.

- If the upper rivulet located at $\theta_u = 50^\circ$ to 65° , the shear layer separated from the upper rivulet can reattach on the upper surface of the cylinder. The reattachment of the separated shear layer causes strong negative pressure on the upper surface of the cylinder, which results in a high non-zero mean lift of the cylinder and potentially induces the occurrence of RWIV.

- From friction coefficient distribution of the cylinder, a negative friction region was observed at the rear of the rivulet, which suggests the existence of separation bubbles at the rear of the rivulet. The separation bubble is intrinsically an unsteady flow phenomenon triggered by the upper rivulet. A serial of small eddies first appears in the laminar shear layer separated from the upper rivulet, which then coalesces and reattaches on the side surface of the cylinder and eventually shed to the wake at the rear of the circular cylinder.

It should be mentioned that the assumption that the shape of rivulet keeps unchanged is adopted in the present study. Actually, during the occurrence of the RWIV, the shape of rivulet is changing as it oscillates circumferentially on the cable surface. Therefore, the effects of the rivulet's shape on the aerodynamic forces of the rivulet and the cable should be clarified in the future study.

Acknowledgments

We are thankful for the grants from National Natural Science Foundation of PRC (51578330), Innovation Program of Shanghai Municipal Education Commission (14YZ004) and Natural Science Foundation of Shanghai (14ZR1416000).

References

- Achenbach, E. (1968), "Distribution of local pressure and skin friction around a circular cylinder in cross-flow up to $Re = 5 \times 10^6$ ", *J. Fluid Mech.*, **34**(4), 625-639.
- Acampora, A. and Georgakis, C.T. (2011), "Recent monitoring of the Øresund Bridge: Observations of rain-wind-induced cable vibrations", *Proceedings of the 13th International Conference on Wind Engineering*, Amsterdam, Netherlands, July.
- Behara, S. and Mittal, S. (2011), "Transition of the boundary layer on a circular cylinder in the presence of a trip", *J. Fluid. Struct.*, **27**(5), 702-715.
- Bi, J.H., Wang, J., Shao, Q., Lu, P., Guan, J. and Li, Q.B. (2013), "2D numerical analysis on evolution of water film and cable vibration response subject to wind and rain", *J. Wind Eng. Ind. Aerod.*, **121**(1), 49-59.
- Breuer, M. (1998), "Numerical and modeling influences on large eddy simulations for the flow past a circular cylinder", *Int. J. Heat Fluid Fl.*, **19**(5), 512-521.
- Cantwell, B. and Coles, D. (1983), "An experimental study of entrainment and transport in the turbulent near wake of a circular cylinder", *J. Fluid Mech.*, **136**, 321-374.
- Cao, Y. and Tamura, T. (2015), "Numerical investigations into effects of three-dimensional wake patterns on unsteady aerodynamic characteristics of a circular cylinder at $Re = 1.3 \times 10^5$ ", *J. Fluid. Struct.*, **59**, 351-369.
- Cosentino, N., Flamand, O. and Ceccoli, C. (2003), "Rain-wind induced vibration of inclined stay cables, part I: experimental investigation and physical explanation", *Wind Struct.*, **6**(6), 471-484.
- Du, X.Q., Gu, M. and Chen, S.R. (2013), "Aerodynamic characteristics of an inclined and yawed circular cylinder with artificial rivulet", *J. Fluid. Struct.*, **43**(6), 64-82.
- Flamand, O. (1995), "Rain-wind induced vibration of cables", *J. Wind Eng. Ind. Aerod.*, **57**(2-3), 353-362.
- Geurts, C.P.W. and Staalduin, P.C.V. (1999), "Estimation of the effects of rain-wind induced vibration in the design stage of inclined stay cables", *Proceedings of 10th International Conference on Wind Engineering*, vol. 2, Copenhagen, Denmark, 21-24 June.
- Gu, M. (2009), "On wind-rain induced vibration of cables of cable-stayed bridges based on quasi-steady assumption", *J. Wind Eng. Ind. Aerod.*, **97**(7-8), 381-391.
- Gu, M. and Du, X.Q. (2005), "Experimental investigation of rain-wind-induced vibration of cables in cable-stayed bridges and its mitigation", *J. Wind Eng. Ind. Aerod.*, **93**(1), 79-95.
- Gu, M., Du, X.Q. and Li, S.Y. (2009), "Experimental and Theoretical simulations on wind-rain induced vibration of 3-D rigid stay cables", *J. Sound Vib.*, **320**(1-2), 184-200.
- Gu, M. and Huang, L. (2008), "Theoretical and experimental studies on aerodynamic instability of 2-dimensional circular cylinder with moving attachment", *J. Fluid. Struct.*, **24**(24), 200-211.
- Gu, M., Liu, C.J., Lou, G.Q., Lin, Z.X. and Xiang, H.F. (1998), "Rain-wind induced vibration of cables on cable-stayed bridges and its control (in Chinese)", *Shanghai J. Mech.*, **19**(4), 281-288.
- Gu, M. and Lu, Q. (2001), "Theoretical analysis of wind-rain induced vibration of cables of cable-stayed bridges", *J. Wind Eng.*, **89**(6), 125-128.
- Jing, H., Xia, Y., Li, H., Xu, Y. and Li, Y. (2015), "Study on the role of rivulet in rain-wind-induced cable vibration through wind tunnel testing", *J. Fluid. Struct.*, **59**(10), 316-327.
- Hikami, Y. and Shiraishi, N. (1988), "Rain-wind induced vibrations of cables stayed bridges", *J. Wind Eng. Ind. Aerod.*, **29**(1-3), 409-418.
- Jing, H.Q., Xia, Y., Li, H., Xu, Y.L. and Li, Y.L. (2017), "Excitation mechanism of rain-wind induced cable vibration in a wind tunnel", *J. Fluid. Struct.*, **68**, 32-47.
- Lemaitre, C., Hémon, P. and Langre, E.D. (2007), "Thin water film around a cable subject to wind", *J. Wind Eng. Ind. Aerod.*, **95**(9-11), 1259-1271.
- Li, H., Chen, W.L., Xu, F., Li, F.C. and Ou, J.P. (2010), "A numerical and experimental hybrid approach for the investigation of aerodynamic forces on stay cables suffering from rain-wind induced vibration", *J. Fluid. Struct.*, **26**(7-8), 1195-1215.
- Li, S., Chen, Z., Wu, T. and Kareem, A. (2013), "Rain-wind-induced in-plane and out-of-plane vibrations of stay cables", *J. Eng. Mech.*, **139**(12), 1688-1698.
- Main, J.A. and Jones, N.P. (1999), "Full-scale measurements of stay cable vibration", *Proceedings of the 10th International Conference on Wind Engineering*, Copenhagen, Denmark.
- Matsumoto, M., Shiraishi, N., Kitazawa, M. et al. (1990), "Aerodynamic behavior of inclined circular cylinders-cable aerodynamics", *J. Wind Eng. Ind. Aerod.*, **33**(1), 63-72.
- Matsumoto, M., Shiraishi, N. and Shirato, H. (1992), "Rain-wind

- induced vibration of cables of cable-stayed bridges”, *J. Wind Eng. Ind. Aerod.*, **43**(1-3), 2011-2022.
- Matsumoto, M., Yagi, T., Sakai, S., Ohya, J. and Okada, T. (2005), “Steady wind force coefficients of inclined stay cables with water rivulet and their application to aerodynamics”, *Wind Struct.*, **8**(2), 107-120.
- Ni, Y.Q., Wang, X.Y., Chen, Z.Q. and Ko, J.M. (2007), “Field observations of rain-wind induced cable vibration in cable-stayed Dongting Lake Bridge”, *J. Wind Eng. Ind. Aerod.*, **95**(5), 303-328.
- Nishimura, H. and Taniike, Y. (2001), “Aerodynamic characteristics of fluctuating forces on a circular cylinder”, *J. Wind Eng. Ind. Aerod.*, **89**(7-8), 713-723.
- Peil, U. and Dreyer, O. (2007), “Rain-wind induced vibrations of cables in laminar and turbulent flow”, *Wind Struct.*, **10**(1), 83-97.
- Schewe, G. (1983), “On the force fluctuations acting on a circular cylinder in crossflow from subcritical up to transcritical Reynolds numbers”, *J. Fluid Mech.*, **133**(133), 265-285.
- Shi, J.J. and Gu, M. (2003), “Wind induced vibration of cables of Nanjing No. 2 Bridge over Yangtze River Research Report”, *Department of Bridge Engineering*, Tongji University (in Chinese).
- Smagorinsky, J. (1963), “General circulation experiments with the primitive equations: I. the basic experiment”, *Mon. Weather Rev.*, **91**(3), 99-164.
- Taylor, I.J. and Robertson, A.C. (2011), “Numerical simulation of the airflow-rivulet interaction associated with the rain-wind induced vibration phenomenon”, *J. Wind Eng. Ind. Aerod.*, **99**(9), 931-944.
- Verwiebe, C. and Rucheweyh, H. (1998), “Wind- and rain-induced oscillations of cable of cable-stayed bridge”, *J. Wind Eng. Ind. Aerod.*, **74-76**, 1005-1013.
- Wang, J., Lu, P., Bi, J.H., Guan, J. and Qiao H.Y. (2016), “Three-phase coupled modelling research on rain-wind induced vibration of stay cable based on lubrication theory”, *J. Fluid. Struct.*, **63**, 16-39.
- West, G.S. and Apelt, C.J. (1982), “The effects of tunnel blockage and aspect ratio on the mean flow past a circular cylinder with Reynolds numbers between 10^4 and 10^5 ”, *J. Fluid Mech.*, **114**, 361-377.
- Xu, Y.L. and Wang, L.Y. (2003), “Analytical study of wind-rain-induced cable vibration: SDOF model”, *J. Wind Eng. Ind. Aerod.*, **91**(1-2), 27-40.
- Xu, Y.L., Li, Y.L., Shum, K.M., Kwok, K.C.F., Kwok, K.C.S. and Hitchcock, P.A., (2006), “Aerodynamic coefficients of inclined circular cylinders with artificial rivulet in smooth flow”, *Adv. Struct. Eng.*, **9**(2), 265-278.
- Yamaguchi, H. (1990), “Analytical study on growth mechanism of rain vibration of cables”, *J. Wind Eng. Ind. Aerod.*, **33**(1-2), 73-80.
- Zdravkovich, M.M. (1990), “Conceptual overview of laminar and turbulent flows past smooth and rough circular cylinders”, *J. Wind Eng. Ind. Aerod.*, **33**(1), 53-62.
- Zdravkovich, M.M. (1997), “Flow around Circular Cylinders”, Vol. 1, Oxford Science Publications, Oxford.
- Zuo, D. and Jones, N.P. (2010), “Interpretation of field observations of wind- and rain-wind-induced stay cable vibrations”, *J. Wind Eng. Ind. Aerod.*, **98**(2), 73-87.